

See discussions, stats, and author profiles for this publication at: <https://www.researchgate.net/publication/228909617>

Infrared Ellipsometry of Self-Assembled Octadecylmercaptan on Gold Films and Nanoislands: Effects of Thickness and Morphology of the Gold Layer

ARTICLE *in* THE JOURNAL OF PHYSICAL CHEMISTRY B · NOVEMBER 2004

Impact Factor: 3.3 · DOI: 10.1021/jp0471305

CITATIONS

10

READS

27

5 AUTHORS, INCLUDING:



Eliza Hutter

McGill University

32 PUBLICATIONS 2,599 CITATIONS

SEE PROFILE



Dipankar Roy

Clarkson University

131 PUBLICATIONS 2,543 CITATIONS

SEE PROFILE

Infrared Ellipsometry of Self-Assembled Octadecylmercaptan on Gold Films and Nanoislands: Effects of Thickness and Morphology of the Gold Layer

D. C. Bradford,[‡] E. Hutter,[‡] K. A. Assiongbon,[¶] J. H. Fendler,^{*,‡,¶} and D. Roy^{*,¶,⊥}

Center for Advanced Materials Processing and Department of Physics, Clarkson University,
Potsdam, New York 13699

Received: June 30, 2004; In Final Form: August 24, 2004

Infrared spectroscopic ellipsometry (IRSE) of organic self-assembled monolayers (SAMs) commonly uses the external reflection geometry and a three-phase system (bulk substrate, SAM, and ambient medium). In the present work, we study a four-phase system for IRSE, where a gold substrate film is sandwiched between a CaF₂ prism and a SAM of octadecylmercaptan (ODM). This sample configuration can be employed for internal reflection IRSE (using a continuous Au film), as well as to boost the detection sensitivity of IRSE through surface-enhanced infrared absorption (using discontinuous film of Au nanoislands). We study how the thickness and morphology of the Au layer in the four-phase structure affect the IRSE results for ODM by using three Au substrates: an optically thick ~ 1000 Å continuous film, a continuous ~ 230 Å thick film, and a discontinuous ~ 220 Å thick film of Au nanoislands. The spectral features of ODM in the last case are different from those of the first two, and are associated with surface-enhanced IRSE. Surface morphologies of the Au substrates are characterized by scanning electron microscopy. The IRSE results are discussed with use of currently known theoretical considerations for differential spectroscopy.

1. Introduction

Spectroscopic infrared ellipsometry (IRSE) has increasingly been recognized as a powerful tool for the characterization of nanostructures, in general, and self-assembled monolayers (SAMs), in particular.^{1–14} This technique has certain advantages over the conventional Fourier transform infrared reflection–absorption spectroscopy (FT-IRRAS).^{15–18} First, IRSE is superior to multiple reflectance measurements in determining the dielectric functions of samples down to submonolayer thickness in the high reflectance wavelength region. Second, and more importantly, IRSE (unlike FT-IRRAS) can measure *both* absorbance and phase effects of thin-film samples. Thus, IRSE provides additional experimental (phase) parameters to FT-IRRAS that can be quantitatively compared with theoretical models. By noting these utilities of IRSE, and considering their potential applications in the investigation of nanostructured multilayers, a number of groups,^{2–14} including our own,¹ are now exploring the possibility for further expansion of the current capabilities of this technique. In our present report, we focus on certain aspects of this issue, and demonstrate that the thickness and morphology of the supporting solid substrate for sample SAMs are crucial factors for exploring further applications of IRSE.

A survey of the published IR studies of organic SAMs¹ indicates that further expansion of IRSE would be particularly useful in the following two areas: (i) combination of both external and internal reflection geometries in IRSE^{10,19} and (ii) incorporation of surface-enhanced infrared reflection–absorption

spectroscopy (SEIRRAS)¹⁹ in the framework of IRSE.^{8,11} We have recently demonstrated how the capabilities of FT-IRRAS can be expanded by combining external and attenuated total internal reflection (ATR) measurements. Using IRSE in such a dual-configuration setup could further facilitate the objectives of this approach. Similarly, the signal enhancement (often up to 100-fold) obtained through surface enhancement of optical fields could significantly improve the detection capability of IRSE for studying very thin SAMs.^{20,22,24}

ATR requires that the Au substrate be sandwiched as a film between an internal reflection element (like a right-angled or hemispherical prism in the Kretschmann configuration) and the sample SAM.^{1,17,18} This Au layer should also be thin enough to allow for a significant evanescent field at the Au-SAM boundary. The tasks of data collection and analysis are considerably simplified if Au substrates used for ATR are fabricated as *continuous* smooth films. On the other hand, SEIRA requires thin but *discontinuous* rough films containing Au (or Ag) nanoislands.²⁰ In the present work, using a model SAM of octadecylmercaptan (ODM), we study how these structural factors of the substrate affect the observations of IRSE. To do this, we first calculate the optimum substrate thicknesses for internal and external reflection IRSE measurements. Subsequently, Au substrates, fabricated according to the theoretically calculated specifications, are used for IRSE experiments. Our experiments will focus on external reflection IRSE, using a sample geometry (an ATR prism, a gold substrate, and a probe SAM in a multilayer configuration) that can be employed for both ATR and external reflection measurements. We examine how the results obtained for a thin Au substrate (~ 230 Å, appropriate for ATR) compare with those for a thick substrate (~ 1000 Å, optically behaving as bulk Au). In addition, we investigate how the spectral features of the adsorbed SAM changes when enhanced optical absorption in the SAM is activated by using a ~ 220 Å thick islandlike rough film of Au.

* Address correspondence to these authors.

[‡] Center for Advanced Materials Processing, Box 5814.

[¶] Department of Physics, Box 5820.

[¶] E-mail: fendler@clarkson.edu. Phone: (315) 268 7113. Fax: (315) 268-4416.

[⊥] E-mail: samoy@clarkson.edu. Phone: (315) 268 6676. Fax: (315) 268-6610.

A brief theoretical discussion of certain aspects of differential reflection spectroscopy that form the basis for data analysis in IRSE is also presented.

2. Theoretical Considerations

Reflection–Absorption Spectroscopy Involving the Optical Density Function. A number of recent IRSE studies have used the complex optical density formalism^{1–3} that is also adapted in our present study. Let us briefly outline the essential features of this formalism. Traditional external reflection FT-IRRAS of organic films uses a three-phase system containing a solid substrate, the sample film and, the ambient medium. For IRSE, we consider a four-phase structure, denoted as (1234), which contains (1) a CaF₂ prism (transparent ATR element in the IR), (2) a gold film substrate, (3) the sample SAM, and (4) the ambient medium. The Fresnel reflection factor for this system is written as^{25,26}

$$r_{1234}^{\gamma} = \frac{a_{123}^{\gamma} + b_{123}^{\gamma} r_{34}^{\gamma} \exp(2i\beta_3)}{c_{123}^{\gamma} + d_{123}^{\gamma} r_{34}^{\gamma} \exp(2i\beta_3)} \quad (1)$$

where γ denotes the polarization state of the probe light; $i = \sqrt{-1}$; r_{lm}^{γ} is the Fresnel reflection factor for the interface between media l and m ($l, m = 1-4$); $r_{lm}^{\gamma} = (a_{lm}^{\gamma} - b_{lm}^{\gamma}) / (a_{lm}^{\gamma} + b_{lm}^{\gamma})$; $a_{lm}^{\gamma} = (\hat{n}_l \cos \theta_l)$; $b_{lm}^{\gamma} = (\hat{n}_m \cos \theta_m)$; $a_{lm}^p = (\hat{n}_m \cos \theta_l)$; $b_{lm}^s = (\hat{n}_l \cos \theta_m)$; $\beta_l = (2\pi \hat{n}_l / \lambda) d_l \cos \theta_l$; λ is the (vacuum) photon wavelength; θ_l is the angle of the optical incidence in medium l ; d_l is the thickness of the l th layer; \hat{n}_l is the complex refractive index ($\hat{n}_l = n_l + i\kappa_l$) of phase l ; n_l and κ_l are the real imaginary parts of \hat{n}_l , respectively; the real (ϵ_{lr}) and imaginary (ϵ_{li}) parts of the complex dielectric function of layer l are related to n_l and κ_l ; $\epsilon_{lr} = n_l^2 - \kappa_l^2$, and $\epsilon_{li} = 2n_l\kappa_l$; $a_{123}^{\gamma} = r_{12}^{\gamma} + r_{23}^{\gamma} \exp(2i\beta_2)$; $b_{123}^{\gamma} = r_{12}^{\gamma} r_{23}^{\gamma} + \exp(2i\beta_2)$; $c_{123}^{\gamma} = 1 + r_{12}^{\gamma} r_{23}^{\gamma} \exp(2i\beta_2)$; $d_{123}^{\gamma} = r_{23}^{\gamma} + r_{12}^{\gamma} \exp(2i\beta_2)$. A similar expression of the Fresnel coefficient r_{124}^{γ} for the SAM-free sample can be obtained by setting $d_3 = 0$ and $\epsilon_3 = \epsilon_4$ in eq 1. Introducing the effective phase angles, δ_{1234}^{γ} for system (1234) with the SAM and δ_{124}^{γ} for system (124) without the SAM, we write

$$r_{1234}^{\gamma} = |r_{1234}^{\gamma}| \exp(i\delta_{1234}^{\gamma}) \text{ and } r_{124}^{\gamma} = |r_{124}^{\gamma}| \exp(i\delta_{124}^{\gamma}) \quad (2)$$

The polarization-dependent reflectances for the four- and three-phase structures are written as $R_{1234}^{\gamma} = |r_{1234}^{\gamma}|^2$ and $R_{124}^{\gamma} = |r_{124}^{\gamma}|^2$, respectively. In traditional FT-IRRAS, the absorbance of the sample SAM layer is often expressed (in notations adapted from transmission experiments) as^{17,27–29}

$$A^{\gamma} = \ln \left[\frac{R_{124}^{\gamma}}{R_{1234}^{\gamma}} \right] \quad (3)$$

In differential reflectance spectroscopy, one deals with the polarization-dependent complex optical density function, D^{γ} , defined as³⁰

$$D^{\gamma} = \ln \left(\frac{r_{124}^{\gamma}}{r_{1234}^{\gamma}} \right) \quad (4)$$

The differential optical density function, D , is written as^{30,31}

$$D = (D^p - D^s) = \ln \left(\frac{r_{124}^p r_{1234}^s}{r_{1234}^p r_{124}^s} \right) \quad (5)$$

Using eqs 2–5, we obtain the real (Re) and imaginary (Im) parts of D :¹

$$\text{Re}D = \frac{1}{2} \left[\ln \left(\frac{R_{124}^p}{R_{1234}^p} \right) - \ln \left(\frac{R_{124}^s}{R_{1234}^s} \right) \right] = \frac{1}{2} (A^p - A^s) \quad (6)$$

$$\text{Im}D = (\Delta_{124} - \Delta_{1234}) \quad (7)$$

where Δ_{1234} and Δ_{124} are relative phase retardations for the SAM-containing and the SAM-free systems, respectively, and are defined as^{32,33}

$$\Delta_{1234} = \delta_{1234}^p - \delta_{1234}^s \text{ and } \Delta_{124} = \delta_{124}^p - \delta_{124}^s \quad (8)$$

The first equality sign in eq 6 highlights the equivalence of the expected signal-to-noise between FT-IRRAS and IRSE in determining the polarization-dependent reflectivity ratios, where the polarization-independent contribution to the response is assumed to be constant. In conventional FT-IRRAS, the terms A^p and A^s can be measured separately to obtain $\text{Re}D$, but measuring $\text{Im}D$ with this method is not possible. FT-IRRAS would not contain any phase information, because the latter is contained in $\text{Im}D$. In IRSE, it is possible to measure both $\text{Re}D$ and $\text{Im}D$ as outlined below.

Optical Density Spectra in Terms of Ellipsometry Parameters. In ellipsometry, one measures two sets of parameters (so-called ellipsometric parameters), namely, the phase retardation (Δ) and the polarization ratio (ψ), and each parameter is determined for both the (124) and (1234) systems. The phase-retardation factor is defined in eq 8. The polarization ratio is defined as^{32,33}

$$\psi_{1234} = \tan^{-1} \left[\frac{|r_{1234}^p|}{|r_{1234}^s|} \right], \text{ and } \psi_{124} = \tan^{-1} \left[\frac{|r_{124}^p|}{|r_{124}^s|} \right] \quad (9)$$

for the (1234) and (124) systems, respectively. In traditional ellipsometry, the Δ and ψ parameters are combined to determine the complex polarization ratios,

$$\rho_{1234} = \frac{r_{1234}^p}{r_{1234}^s} = \tan(\psi_{1234}) \exp(i\Delta_{1234}) \text{ and } \rho_{124} = \frac{r_{124}^p}{r_{124}^s} = \tan(\psi_{124}) \exp(i\Delta_{124}) \quad (10)$$

for the (1234) and (124) systems, respectively. The optical density function can be expressed now as $D = \ln(\rho_{124}/\rho_{1234})$, so that using eq 10,

$$\text{Re}D = \ln \left(\frac{\tan(\psi_{124})}{\tan(\psi_{1234})} \right) \quad (11)$$

and $\text{Im}D$ is still given by eq 7.

In IRSE, ψ_{124} , ψ_{1234} , Δ_{124} , and Δ_{1234} are measured in the wavelength region where vibrational signatures of the sample SAM are expected.² Subsequently, wavelength-dependent $\text{Re}D$ and $\text{Im}D$ are determined by using eqs 11 and 7. In systems where the surface selection rule ($R_{1234}^s \approx R_{124}^s$) of IR absorption is active, $\text{Re}D$ simply represents the p-polarized reflection absorption spectrum. The corresponding $\text{Im}D$ data represent a “phase spectrum” of the IR absorbing sample. Both $\text{Re}D$ and $\text{Im}D$ are functions of n_3 , κ_3 , and d_3 of the SAM, as well as of the average orientation angle of the SAM with respect to the surface normal. The latter set of parameters can be obtained by fitting measured spectra of $\text{Re}D$ and $\text{Im}D$ to appropriate

multilayer reflectivity models. Analysis of IRSE data using the latter approach has been reported by previous authors,^{2–14} and will not be considered in our present paper. Instead, we will focus here on probing the substrate-structure dependent overall features of the optical density spectra.

3. Experimental Section

Gold films were deposited on CaF₂ slides (cleaned by water and ethanol and dried by gaseous nitrogen) in an Edwards AUTO306 compact vacuum coater by evaporation of gold shots under high vacuum (typically 10^{−6} Torr, i.e., 0.76 × 10^{−9} atm). The CaF₂ substrates were placed at a distance of 10.5 cm from the metal sources. The temperature in the chamber remained below 40 °C. The thickness and deposition rate of the films were monitored with a built-in system consisting of a quartz crystal mechanically oscillating at its natural resonance frequency (6 MHz). The deposited mass and the film thickness were calculated from the change of oscillation frequency of the quartz crystal. The structure of the film (continuous or islandlike) was controlled by the rate of deposition. The films were stored in a desiccator and used within days following their fabrication. SEM images of the films prior and after self-assembly of monolayer were taken on a JEOL JSM-7400F instrument. Image analysis software ("Image J", version 1.32j) was used to quantify the islandlike nature of the ultrathin film (~216 Å) that was deposited under predesigned conditions for a discontinuous film. The gold films were cleaned thoroughly with water and ethanol, then immersed into a 1 mM ethanolic solution of ODM for 1 h, followed by thorough washing with water and ethanol and drying with nitrogen.

IR spectra were recorded with a Digilab FTS 7000 spectrometer in rapid scan mode at 20 kHz, using an undersampling ratio of 2, and co-adding 256 scans. In an external sample compartment, a gold grid polarizer was used to obtain the linearly polarized incident radiation, set at 45° to the plane of incidence with an angle of incidence of 70°. A second gold grid polarizer was set at 0° (p), 90° (s), or −45° between the sample and a liquid nitrogen cooled narrow band HgCdTe (MCT) detector for the data sets needed for ellipsometry. The formulas necessary for converting the reflectivities measured in this approach to the ellipsometric ψ and Δ (technically $|\Delta|$) parameters have been discussed in detail in ref 2. A slightly different formula for Δ was derived necessitated by our using an azimuthal angle of the analyzer at −45° instead of +45°, and to explicitly show dependence on the raw reflectance data, independent of ψ

$$\psi = \frac{1}{2} \cos^{-1} \left(\frac{I_s - I_p}{I_s + I_p} \right) \text{ and } \Delta = \cos^{-1} \left(\frac{I_s + I_p - 2I_{-45}}{2\sqrt{I_s I_p}} \right) \quad (12)$$

where I_s , I_p , and I_{-45} are the measured intensities at analyzer azimuthal angles of 90°, 0°, and −45°, respectively. We note here that the characteristic nonlinear response of MCT detectors could sometimes be problematic in conventional reflectivity measurements. In the above-mentioned framework of IRSE analysis, however, we only examine the polarization-dependent variations of the optical signal, and the polarization-independent component of the signal (that is intrinsic to the MCT detector) is eliminated from the processed data (ψ and Δ). In our IRSE measurements, the convention used for rotations of the electric field vector relative to the plane of incidence was positive for counterclockwise rotations looking in the direction of the propagation vector. A 90° rotation of the analyzer relative to the incident beam produced the largest of the three signals as

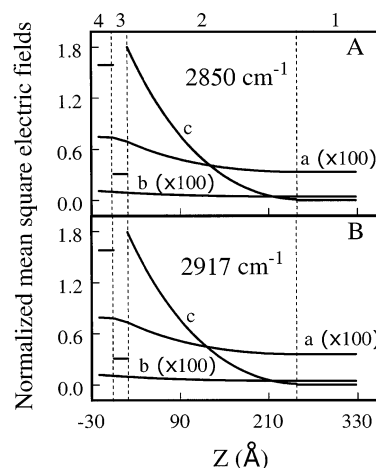


Figure 1. Calculated optical field profiles in a four-phase system containing (1) a CaF₂ prism, (2) a continuous Au film (229 Å), (3) a SAM of ODM (17 Å), and (4) air. The mean square field in phase 1 for s-polarization is (b) $\langle E_s^2 \rangle$, and those for labeled p-polarization are (a) $\langle E_t^2 \rangle$ and (c) $\langle E_p^2 \rangle$. The angle of incidence (in external reflection) is 70°, and the absorption wavenumbers are (A) 2850 and (B) 2917 cm^{−1}. All fields are normalized with respect to the x-component of the incident field in air.

expected for near grazing angle reflections from metallic substrates. The width (2 cm^{−1}) of the aperture, the instrument resolution (4 cm^{−1}), and the detector sensitivity (1) were kept fixed in all experiments. Each set of three scans was taken as close together as possible allowing for, on average, a half hour of purge time for the FTS 7000 and external experimental chamber with a Parker Balston purge gas generator.

4. Results and Discussion

Calculated Optical Field Profiles. As we mentioned in Section 1, the thickness of the Au substrate is a crucial factor in the four-phase sample design for dual-configuration (external reflection and ATR) IR spectroscopy of organic SAMs. The Au layer must be thin enough for ATR (radiation incident from phase 1) to avoid excessive IR absorption by the substrate. At the same time, requirements of structural stability set a lower limit (100–150 Å) on the thickness of this Au layer. Moreover, if the Au layer is too thin, the analysis of external reflection measurements (radiation incident from phase 4) may become complicated due to possible multiple reflections at the Au–prism interface. Optimization of the substrate thickness in this work is based on the above considerations, and is achieved through both theoretical calculations and experimental measurements.

Through numerical simulations, we find that a gold layer of ~150–200 Å thickness is appropriate to meet the requirements specified above. Sample optical field profiles, calculated for this optimization of substrate thickness, are shown in Figures 1–3, where we plot the mean square electric fields for s- and p-polarized beams in a four-phase structure for different substrate thicknesses and different reflection geometries. These calculations are based on Hansen's formalism,³⁴ and have been discussed in our earlier work.^{1,21} The plane of incidence is taken to be the x – z plane of a Cartesian system, and the direction of optical transmission is taken along the positive z -direction (pointed from phase 4 to phase 1 for external reflection, and in the opposite direction for ATR). The origin, $z = 0$, locates the interface (4–3 in external reflection with a SAM, and 1–2 in ATR) between the medium of optical incidence and its adjacent phase. The normalized mean square field $\langle E_t^2 \rangle$ for s polarization

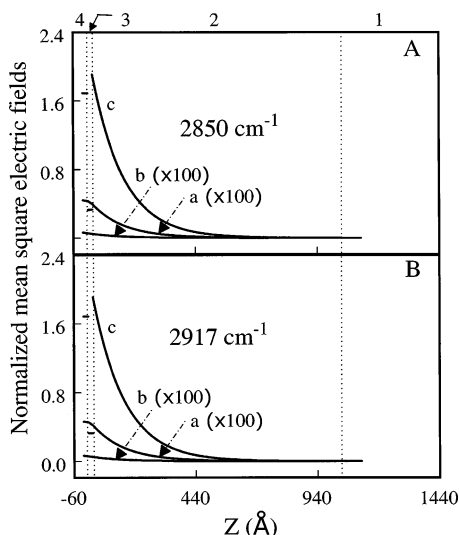


Figure 2. Calculated optical field profiles for external reflection in a four-phase system as considered in Figure 1. The thickness of the Au substrate film is 1021 Å. All other system parameters, as well as the labels and notations for the plots, are the same as those described in Figure 1.

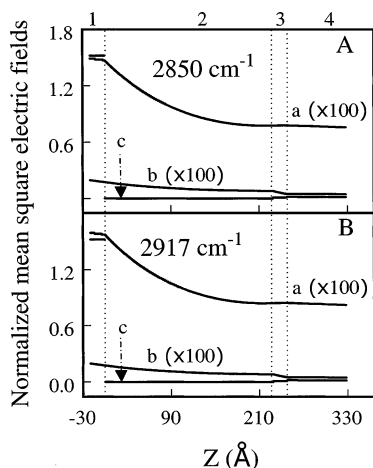


Figure 3. Calculated optical field profiles for internal reflection (at 70° incidence in CaF₂) in the four-phase system considered in Figure 1. The mean square fields for s (plots b) and p (plots a and c) polarization are $\langle E_{ly}^2 \rangle$, $\langle E_{lz}^2 \rangle$, and $\langle E_{lx}^2 \rangle$ (as in Figure 1). The photon wavenumbers are (A) 2850 and (B) 2917 cm⁻¹. All fields are normalized with respect to the x-component of the incident field in CaF₂.

($l \equiv 1-4$) is labeled as plot b; the corresponding fields $\langle E_{lx}^2 \rangle$ and $\langle E_{lz}^2 \rangle$ for p-polarization are labeled as plots a and c, respectively. All these fields are normalized with respect to the x-component of the incident field, and the procedure for this normalization is described elsewhere in detail.^{17,35,36} ODM on Au has two main absorption peaks, located at ~ 2850 (CH₂ symmetric stretching vibration) and ~ 2917 cm⁻¹ (CH₂ asymmetric stretching vibration).²¹ Our calculations are performed at these two relevant photon energies, as shown in panels A and B, respectively, of Figures 1–3. The angle of incidence is set at 70°, along with the optical constants³⁷ listed in the first three rows in Table 1. We also use $d_1 = d_4 = \infty$ and $d_3 = 17$ Å,²¹ and examine two values of d_2 , 229 and 1021 Å (the experimental results presented later in our paper correspond to these two specific values of d_2). As we show in the following, the 229 Å value lies in the region of maximum thickness for the Au film that can be used for ATR. The 1021 Å thick Au

TABLE 1: Optical Parameters for Calculated Results in Figures 1–3

parameter	value at 2850 cm ⁻¹	value at 2917 cm ⁻¹
$\epsilon_{1r}, \epsilon_{1i}$	1.99, 0	1.99, 0
$\epsilon_{2r}, \epsilon_{2i}$	$-4.75 \times 10^2, 93.78$	$-4.50 \times 10^2, 87.16$
$\epsilon_{3r}, \epsilon_{3i}$	2.24, 0.30	2.24, 0.30
$\langle E_{2x}^2 \rangle^c$ at $z = d_3 + d_2$	$3.4 \times 10^{-3}{}^a$	$3.6 \times 10^{-3}{}^a$
$\langle E_{2y}^2 \rangle^c$ at $z = d_3 + d_2$	$5.1 \times 10^{-6}{}^b$	$5.8 \times 10^{-6}{}^b$
$\langle E_{2z}^2 \rangle^c$ at $z = d_3 + d_2$	$4.4 \times 10^{-4}{}^a$	$4.7 \times 10^{-4}{}^a$
$\langle E_{2x}^2 \rangle^d$ at $z = d_2 + d_3$	$1.1 \times 10^{-6}{}^b$	$1.2 \times 10^{-6}{}^b$
$\langle E_{2y}^2 \rangle^d$ at $z = d_2 + d_3$	$1.2 \times 10^{-2}{}^a$	$1.3 \times 10^{-2}{}^a$
$\langle E_{2z}^2 \rangle^d$ at $z = d_2 + d_3$	$2.0 \times 10^{-5}{}^b$	$2.1 \times 10^{-5}{}^b$
$\langle E_{2x}^2 \rangle^d$ at $z = d_2 + d_3$	$7.8 \times 10^{-3}{}^a$	$8.4 \times 10^{-3}{}^a$
$\langle E_{2y}^2 \rangle^d$ at $z = d_2 + d_3$	$4.9 \times 10^{-4}{}^a$	$5.4 \times 10^{-4}{}^a$
$\langle E_{2z}^2 \rangle^d$ at $z = d_2 + d_3$	$1.0 \times 10^{-2}{}^a$	$1.1 \times 10^{-2}{}^a$

^a For $d_2 = 229$ Å. ^b For $d_2 = 1021$ Å. ^c $z = d_3 + d_2$ represents the Au–CaF₂ interface in external reflection (Figures 1 and 2). ^d $z = d_2 + d_3$ represents the SAM–air interface in internal reflection (Figure 3).

film represents the limit where the substrate behaves essentially like bulk Au in external reflection measurements.

In Figures 1–3, the optical response of the experimental system is very similar at the two absorption bands considered (in panels A and B). Moreover, in all cases of Figures 1–3, the surface-normal field $\langle E_{lz}^2 \rangle$ has the maximum value in all four phases considered (both $\langle E_{lx}^2 \rangle$ and $\langle E_{ly}^2 \rangle$ are magnified by a factor of 100). This predominance of the z-directional electric field is responsible for the earlier mentioned surface selection rule. In addition, unlike $\langle E_{lx}^2 \rangle$ and $\langle E_{ly}^2 \rangle$, the normal field $\langle E_{lz}^2 \rangle$ is discontinuous at the phase boundaries as a consequence of electromagnetic boundary conditions. In rows 4–6 of Table 1, we have listed the calculated values of the three field components at the Au side of the Au–air interface for external reflection. A comparison of these values for the two films indicates how the 1021 Å thick film acts almost like bulk Au (allowing negligible amounts of light to pass through Au into the final phase of CaF₂). In comparison, the 229 Å thick film transmits larger amounts of fields into the final medium. The reflected fields in air are practically independent of the different film thicknesses considered in Figures 1 and 2. This implies that for the wavelength region considered here, the overall results of (external) reflectivity measurements should not be strongly affected if we switch over from a bulk gold substrate to a gold film as thin as 229 Å. It is also useful to note here that the normalized electric fields in certain regions in Figures 1–3 exceed the value of unity. This happens because the normalization of fields is performed here with respect to the x-component (not the full magnitude) of the incident field. Similar results have been published previously (as in Figures 11 and 12 of ref 17 and in Figure 16 of ref 36).

A comparison of Figures 2 and 3 indicates that the spatial profiles of the calculated electric fields for internal and external reflection modes are considerably similar; only the optical input and output directions are different in the two cases. The calculated normalized field components at the SAM side of the SAM–air interface in internal reflection are listed in the last three rows of Table 1 (only the 229 Å thick film is considered here). These values show how much of the evanescent field is experienced by the sample SAM. As in the case of external reflection, here again the main measurable field contributions come from the z-directional fields. Considering the decaying fields in the Au phase, we also note in Figure 3 that a thinner Au film (100–150 Å) would provide stronger evanescent fields to the SAM sample, and therefore (setting aside detailed fabrication issues) would be a better choice for ATR measurements.

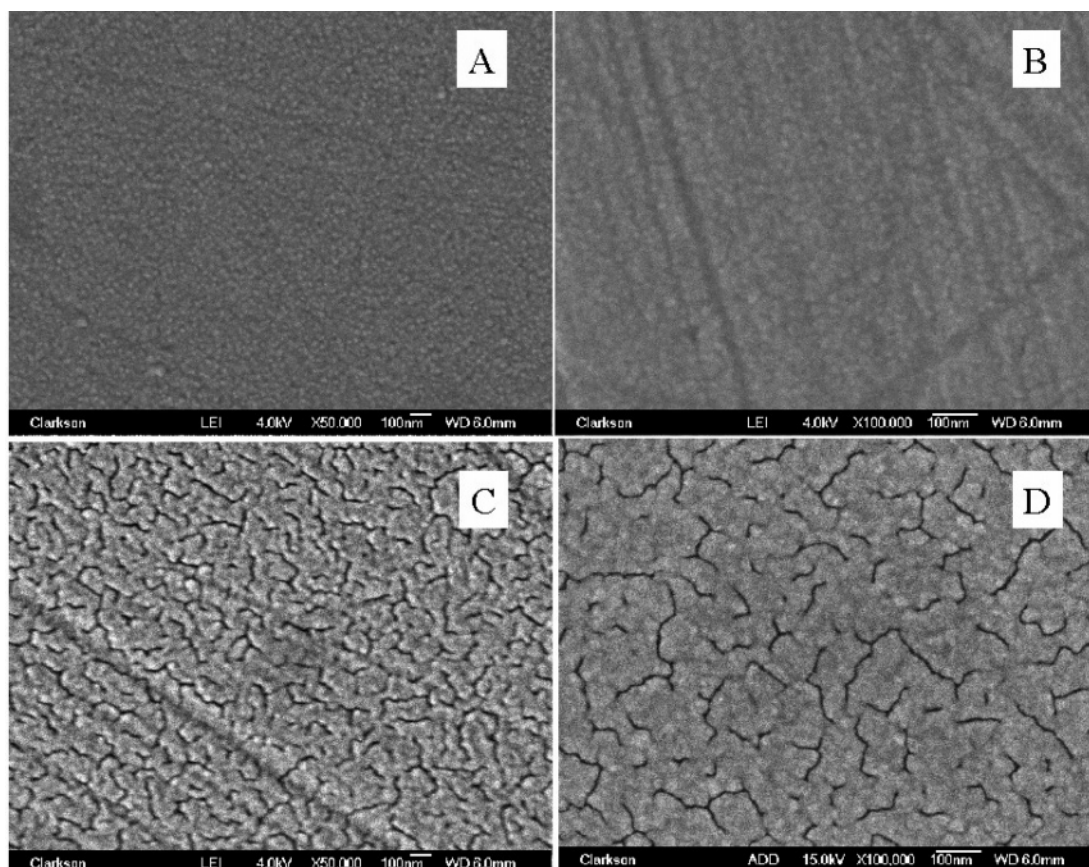


Figure 4. SEM images of continuous (A and B) and nanoisland-containing (C and D) Au film substrates. The thickness of the Au film is 1021 (A), 229 (B) and 216 Å (C and D). Panels C and D show the same island film at two different magnifications.

TABLE 2: Fabrication Conditions and Characteristic Parameters for Gold Substrate Films

type of Au substrate	thickness, Å	rate of deposition, Å s ⁻¹	resistivity, × 10 ⁻⁶ Ω cm ^b
thick continuous film	1021	5.10	4.40
thin continuous film	229 ^a	9.20	7.55
thin island film	216	0.14	18.77

^a Confirmed by surface plasmon resonance measurement. ^b Resistivity of bulk gold is 2.35×10^{-6} Ω cm.

The results of Figures 1–3 show how relatively simple calculations can help to design the appropriate thickness of (continuous) Au substrates for IRSE measurements in external or internal reflection. Similar calculations can be performed for islandlike discontinuous Au films. The latter calculations generally involve an appropriate effective medium approximation (EMA),¹ requiring detailed considerations of various (often unknown) parameters of the EMA. Other authors have reported a number of such calculations for Au nanoislands,^{11,20,38} and therefore, this subject will not be considered here. Instead, we will use experimental results (presented later) for a four-phase system (CaF₂, Au-island film, SAM, air) to examine the optical behavior of Au nanoislands in IRSE.

Surface Morphologies of Continuous and Nanoisland Au Films. Figure 4 shows SEM images of the three thin film Au substrates employed in the present work. The characteristic fabrication and resistivity parameters of these films are listed in Table 2. Surface morphologies of the Au films are found to depend strongly on the rate of gold evaporation onto the substrates. A fast deposition rate, in the range of 5–10 Å s⁻¹, leads to smooth continuous films as indicated by their SEM

images (Figure 4) and their electrical resistivities (Table 1). Conversely, a deposition rate slower than 0.2 Å s⁻¹ leads to the formation of densely packed islands and increased resistivity (Figure 4 and Table 1). This is entirely in accord with what was reported previously.^{23,39} Using the image analysis procedure mentioned in the Experimental Section, we determined 5.5% dark cracks in the SEM image of Figure 4D. The topography of the island film observed in panels C and D of Figure 4 is similar to those reported previously for Au^{40–42} and Ag⁴³ nanoislands deposited at room temperature under experimental conditions similar to those used here. The resistivity of the discontinuous Au film measured here is also similar to those reported in ref 41 for ultrathin discontinuous Au films deposited on glass at room temperature.

Measured Spectra of Ellipsometry Parameters. Figure 5 presents experimental IRSE data in this region for the three-phase (124) sample without the ODM SAM. The spectral segment shown here represents the “blank” spectrum corresponding to the main absorption region of ODM. The dashed and solid lines represent the ellipsometry parameters, ψ_{124} and Δ_{124} , respectively. We note here that we did not perform additional experiments with a retarder to introduce known phase differences between the p and s components of the probe beam. Thus the present measurements are limited to determining the absolute value of Δ . The data in parts A, B and C are recorded by using the three Au substrates shown in Figure 4, panels A, B, and C, respectively. In Figure 6A–C, we present the corresponding spectra of ψ_{1234} (dashed lines) and Δ_{1234} (solid lines), recorded for the four-phase system containing the ODM SAM. The angle of incidence is 70° in both Figures 5 and 6.

Due to the presence of the thick Au substrate in Figure 5A, the (124) system is optically not too different from a two-phase

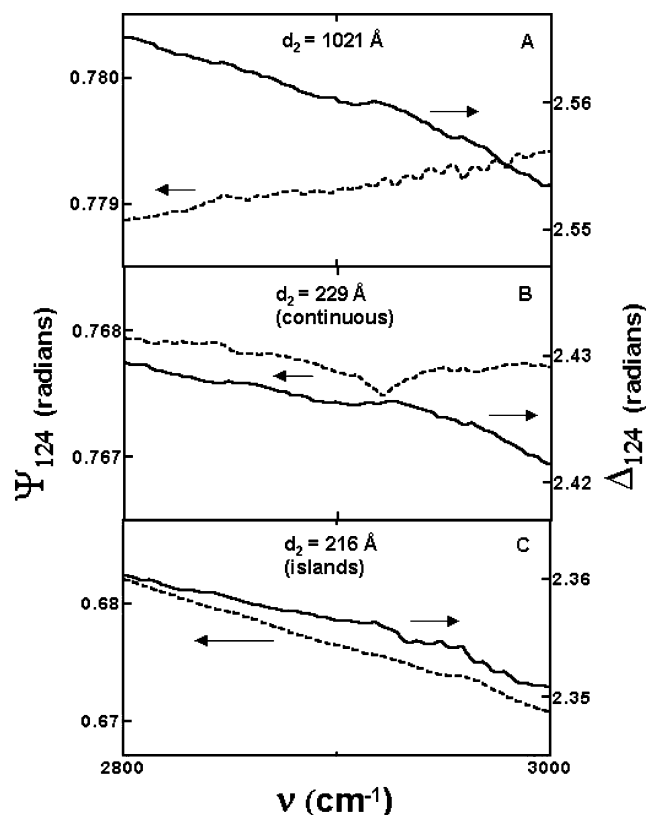


Figure 5. Experimentally measured IR spectra of the ellipsometry parameters (a) ψ_{124} and (b) Δ_{124} for a three-phase structure, which is essentially the same as the multilayer system considered in Figure 6, but does not contain the ODM layer. The substrates used in panels A, B, and C are those shown in Figure 4, panels A, B, and C, respectively.

(24) system characterized by an air–bulk Au interface. For the same reason, the (1234) sample in Figure 6A behaves effectively almost like a three-phase (234) structure. This specific feature of the thick Au substrate is manifested in the relatively higher values of ψ_{124} and ψ_{1234} in Figures 5A and 6A, respectively. The spectra of ψ_{124} and Δ_{124} for the SAM-free sample arise from the wavelength-dependent values of n_2 and κ_2 of Au in the given spectral region. The absolute values of ψ_{124} and Δ_{124} are somewhat different between panels A and B in Figure 5. This is primarily an effect of some light being reflected from the Au–CaF₂ interface when the 229(±1) Å Au substrate is used (Figure 5B). The high-wavenumber region of the Δ_{1234} plot in Figure 6B shows some weak features of interference. Nevertheless, the overall (featureless) behaviors of the 1021 and 229 Å substrates in panels A and B of Figure 5 are comparable. A comparison of the results in panels A and B of Figure 6 for the (1234) system also indicate comparable optical behaviors of the 1021 and 229 Å continuous Au films.

In eq 9, ψ_{1234} contains direct information about absorption through the “moduli” of the Fresnel reflection coefficients. On the other hand, Δ_{1234} just contains information about phases (“arguments” of the Fresnel reflection coefficients), where usually no strong effects of absorption (vibrational features) are manifested. Thus, for the (1234) structure in Figure 6A, absorption effects of ODM appear mainly in the ψ_{1234} spectrum, and only two weak features of CH₂ vibrations are observed in the Δ_{1234} spectrum. Four absorption features at 2850, 2878, 2918, and 2964 cm^{−1} are noticeable in the ψ_{1234} spectra of both panels A and B in Figure 6, reproducible to within ±1 cm^{−1} for the thick and thin continuous films. The two stronger peaks at 2850 and 2918 cm^{−1} are identified as symmetric and

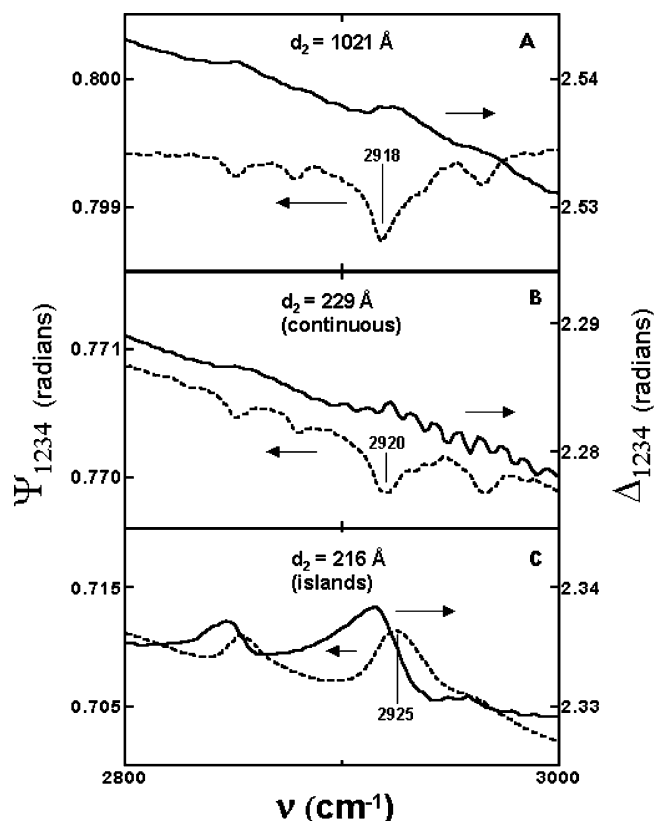


Figure 6. Experimentally measured IR spectra of the ellipsometry parameters (a) ψ_{1234} and (b) Δ_{1234} for the four-phase structure considered in the calculations in Figure 1. The plots in panels A, B, and C of Figure 6 are obtained with the Au substrates used in the corresponding panels of Figure 5. The selected spectral segment corresponds to the region of the main vibrational modes of ODM.

asymmetric CH₂ stretching modes, respectively. The two relatively weaker peaks at 2878 and 2964 cm^{−1} represent symmetric and asymmetric CH₃ stretching modes, respectively. The wavelength-dependent dielectric functions of Au seem to dominate the corresponding Δ_{1234} spectra in Figure 6, panels A and B.

The overall shapes of the ψ_{124} and Δ_{124} spectra for the SAM-free (124) structure involving the rough Au film in Figure 5C are qualitatively comparable to their respective counterparts for the smooth films in panels A and B in Figure 5. However, both the absolute values and the slopes of the ψ_{124} and Δ_{124} plots are somewhat different between the rough and the smooth Au films. In addition, the optical signals in Figure 5C for the rough Au film are considerably enhanced, indicating the presence of SEIRA in this case. This is seen by comparing the signal-to-noise ratios in the ψ_{124} and Δ_{124} plots of Figure 5C with those of Figure 5A,B. These observations can be explained by noting that the Au substrate layer in Figure 5C is effectively a composite film containing both Au nanostructures and air. According to standard effective medium models of composite structures,^{1,33,44,45} the effective values of the real and imaginary refractive indices (n_2^{eff} , κ_2^{eff}) of such a layer are functions of (i) n_2 , (ii) κ_2 , (iii) n_4 , (iii) relative volumes of media 2 and 4 in the composite layer, and (iii) shape and size of the Au nanostructures. Depending on these various factors, the wavelength-dependent n_2^{eff} and κ_2^{eff} can be considerably different than n_2 and κ_2 of smooth Au films.⁴⁵ These differences give rise to the different wavelength dependencies of the ellipsometric parameters for smooth and rough Au films. SEIRA in the presence of Au nanoislands, as observed in the results of Figure 5C,

occurs as a result of excitation of localized surface plasmons within the Au nanoislands.^{1,20} The degree of this enhancement depends on the values of n_2^{eff} and κ_2^{eff} , and hence on all the above-mentioned variables that control the values of n_2^{eff} and κ_2^{eff} . Previous authors have discussed various aspects of such SEIRA effects in considerable detail.^{11,20,38}

The results for the ODM-containing (1234) system in Figure 6C contain the essential signatures (strong signal) of SEIRA already observed in Figure 5C. The wavelength-dependent background signals (underlying the observed vibrational features) of ψ_{1234} and Δ_{1234} in Figure 6C are similar to their respective spectra in Figure 5C. Compared to the cases of Figure 6A,B, the signatures of CH_2 vibrations in Δ_{1234} and ψ_{1234} spectra of Figure 6C are optically enhanced almost by an order of magnitude. The main peaks in Figure 6C, however, are somewhat broadened, and tend to mask the relatively weaker peaks of CH_3 vibrations. A strong contribution to this latter effect is likely to come from the heterogeneity of adsorption sites for ODM on the rough Au surface of Figure 6C. An important result of Figure 6C is that (unlike Figure 6A,B) here the two main vibrational features of ODM are visible not only in the ψ_{1234} spectrum, but also in the Δ_{1234} spectrum. This shows that any absorption-sensitive features of Δ_{1234} , which are normally subdued compared to those of ψ_{1234} in the “unenanced” spectra for continuous films, are clearly brought out by the Au island-supported optical enhancement. Thus, for systems associated with weak absorption signals, discontinuous Au substrate films may in fact be more advantageous than continuous substrates for identifying the signature CH_2 stretching modes of the probe molecules used.

In Figure 6, the spectra for ψ_{1234} and Δ_{1234} are interdependent through the Kramers–Kronig relation.³² Thus, an approximately bell-shaped feature (of the main CH_2 vibration) in the second spectrum leads to a dispersion-like structure in the first spectrum. The dispersion curve is nearly symmetric around the spectral position of the absorption band. The Δ_{1234} term closely mimics the wavelength dependence of the real refractive index (n_3) of the SAM.^{32,45} This can be seen here by comparing the three solid line plots in panels A, B, and C in Figure 6, where the main signature feature (weak in A and B and well-defined in C) of the SAM in the Δ_{1234} spectrum for the three substrates appears essentially at the same wavenumber. The same feature of ψ_{1234} (inverted in A and B and upright in C) shifts to higher wavenumbers as the Au substrate becomes thinner. This shows the selective sensitivity of Δ_{1234} toward the wavelength dependence of n_3 , and a similar predominant sensitivity of ψ_{1234} toward variations in the substrate thickness.

The peaks in the ψ_{1234} spectrum in Figure 6C are “inverted” with respect to those observed in Figure 6A,B. According to eq 9, this implies that $|r_{1234}^{\text{p}}|$ increases relative to $|r_{1234}^{\text{s}}|$ in the absorption region of the SAM as we replace the smooth Au substrate in the four-phase structure with the discontinuous Au nanoisland film. Previous authors have observed similar effects of peak inversion in IR absorption measurements.²⁷ It has been suggested^{27,42} that this effect is not intrinsic to the optical enhancement of SEIRA, but is related to changes in the relative values of A^{p} and A^{s} (and, therefore, to changes of the ratio $|r_{1234}^{\text{p}}|/|r_{1234}^{\text{s}}|$) as a result of changing the complex refractive index of the Au substrate from $(n_2 + i\kappa_2)$ to $(n_2^{\text{eff}} + i\kappa_2^{\text{eff}})$. Furthermore, molecular orientation on the nanoisland film should be considered random on a macroscopic scale. Depending on the experimental system, wavelength dependencies of $|r_{1234}^{\text{s}}|$ and $|r_{1234}^{\text{p}}|$ for such a molecular layer (Figure 6C) in the absorption region can be quite different from those observed in

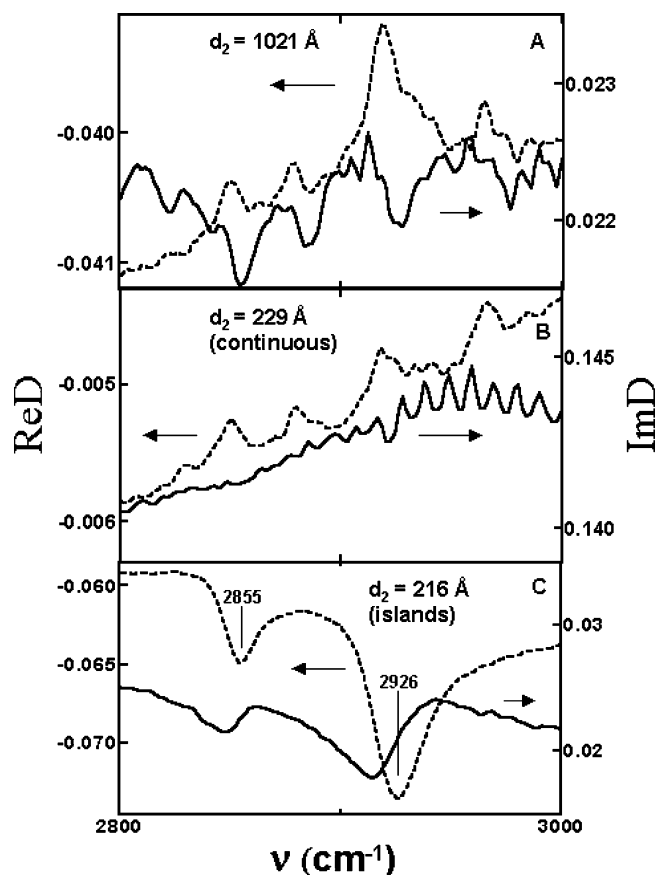


Figure 7. Experimentally measured IR spectra of the real (ReD, dashed lines) and imaginary (ImD, solid lines) complex optical density functions for a SAM of ODM, obtained by using the data from Figures 5 and 6. The Au substrates considered in panels A, B, and C ($d_2 = 1021$, 229, and 216 Å, respectively) are the same as the corresponding panels of Figures 5 and 6.

the case of preferentially oriented molecules on smooth substrates (Figure 6A,B). By modeling surface nanoislands as ellipsoids, Osawa et al. have performed detailed calculations to examine these different factors that contribute to polarization-dependent inversion of IR absorption peaks.²⁰ As we mentioned earlier in this paper, fitting such calculations with experimental data usually involves several unknown parameters, and will not be attempted in the present work. Nevertheless, considering the overall optical response of the Au nanoisland sample, we note here that our results for external reflection IRSE in Figure 7C are similar to those reported previously for external reflection IRRAS of organic molecules adsorbed onto Ag islands.⁴³

Optical Density Spectra from Ellipsometry Data. Figure 7 shows the spectra of ReD (dashed lines) and ImD (solid lines), obtained by using the ellipsometric parameters from Figures 6 and 5 in eqs 11 and 8. In Figure 6A,B we have seen that the SAM absorption features were only weakly manifested in the Δ_{1234} spectra for samples containing the smooth Au films. Thus, in the differential phase spectra represented by ImD for these two samples in Figure 7A,B, the absorption features of ODM are noticeably masked by noise. This situation changes drastically in the enhanced spectra of Figure 7C, where both ReD and ImD contain clearly visible features of CH_2 vibrations. Moreover, as we have already seen in Figure 6, the enhanced spectra in Figure 7C are also inverted with respect to their respective counterparts in Figure 7A,B. We have discussed these effects of the nanoisland Au film in the context of Figure 6.

In Figure 7C, ImD shows the same Kramers–Kronig relation to ReD comparable to that observed between Δ_{1234} and ψ_{1234} (originating parameters of ImD and ReD, respectively) in Figure 6C. A similar relationship between ImD and ReD (although not negative absorption as is seen here) has been found previously in IRSE of hexadecanethiol on Au.² We note in this context that the orientation of an adsorbed functional group strongly affects the value of ReD, whereas ImD depends mostly on the effective optical thickness of the SAM.² Depending on the SAM, this thickness may be relatively insensitive to changes in the orientation of the adsorbate.^{46–48} In such cases, orientation-dependent absorption features of ReD could be different from the corresponding features of ImD.

5. Conclusions

We have shown in this report how IRSE measurements involving organic SAMs are affected by the thickness and surface roughness of the substrate Au layer. By controlling the rate of deposition during its fabrication, a thin Au film of a certain thickness can be designed to have a continuous or a discontinuous nanoisland structure. We have studied three representative cases of different types of substrate thicknesses and morphologies. We used two Au films of very similar thicknesses (~ 220 Å) that have different surface morphologies (roughness). The IR optical density spectra of an ODM SAM anchored by the continuous Au film exhibits features similar to those obtained with an optically thick ~ 1000 Å Au substrate. On the other hand, the islandlike film of essentially the same thickness leads to different spectral features, including surface-enhanced optical absorption and inverted absorption peaks. We have shown that these observations are consistent with presently available theoretical considerations of differential IR spectroscopy. The results presented in this work demonstrate how the utility of IRSE can be expanded by appropriately designing the structure of the SAM-anchoring layer of Au. We have used here ODM as a model SAM to show how substrate-induced optical enhancement is manifested in IRSE. This experimental technique should apply equally well to other alkanethiol SAMs of different molecular lengths.

Acknowledgment. This work was supported by the United States Department of Energy, and by the National Science foundation (Grant No. INT-0206923).

References and Notes

- Roy, D.; Fendler, J. H. *Adv. Mater.* **2004**, *16*, 479–508.
- Meuse, C. W. *Langmuir* **2000**, *16*, 9483–9487.
- Vanderah, D. J.; Pham, C. P.; Springer, S. K.; Silin, V.; Meuse, C. W. *Langmuir* **2000**, *16*, 6527–6532.
- Hinrichs, K.; Röseler, A.; Gensch, M.; Korte, E. H. *Thin Solid Films* **2004**, *455–456*, 266–271.
- Schubert, M.; Bundesmann, C.; Jakopic, G.; Maresch, H.; Arwin, H.; Persson, N.-C.; Zhang, F.; Inganäs, O. *Thin Solid Films* **2004**, *455–456*, 295–300.
- Korte, E.-H.; Röseler, A. *J. Mol. Struct.* **2003**, *661–662*, 579–585.
- Korte, E.-H.; Karsten, H. K.; Röseler, A. *Spectrochim. Acta* **2002**, *B57*, 1625–1634.
- Korte, E.-H.; Röseler, A.; Buskühl, M. *Talanta* **2000**, *53*, 9–16.
- Drevillon, B. *Thin Solid Films* **1998**, *313–314*, 625–630.
- Tiwald, T. E.; Thompson, D. W.; Woollam, J. A.; Pepper, S. V. *Thin Solid Films* **1998**, *313–314*, 718–721.
- Röseler, A.; Korte, E.-H. *Thin Solid Films* **1998**, *313–314*, 732–736.
- Tompkins, H. G.; Tiwald, T.; Bungay, C.; Hooper, A. E. *J. Phys. Chem. B* **2004**, *108*, 3777–3780.
- Tsankov, D.; Hinrichs, K.; Korte, E.-H.; Dietel, R.; Röseler, A. *Langmuir* **2002**, *18*, 6559–6564.
- Garcia-Caurel, E.; Drevillon, B.; De Martino, A.; Schwartz, L. *Appl. Opt.* **2002**, *41*, 7339.
- Dluhy, R. A.; Stephens, S. M.; Widayati, S.; Williams, A. D. *Spectrochim. Acta* **1995**, *51*, 1413.
- Axelsen, P. H.; Citra, M. J. *Prog. Biophys. Mol. Biol.* **1996**, *66*, 227.
- Hansen, W. N. In *Advances in Electrochemistry and Electrochemical Engineering*; Muller, R. H., Ed.; Wiley-Interscience: New York, 1973; Vol. 9, p 1.
- Harrick, N. J. *Internal Reflection Spectroscopy*; Harrick Scientific Corp.: Ossining, NY, 1979.
- Kim, M. W.; Peiffer, D. G.; Chen, W.; Hsiung, H.; Rasing, Th.; Shen, Y. R. *Macromolecules* **1989**, *22*, 2682–2685.
- Osawa, M. *Bull. Chem. Soc. Jpn.* **1997**, *70*, 2861–2880.
- Hutter, E.; Assiongon, K. A.; Fendler, J. H.; Roy, D. *J. Phys. Chem. B* **2003**, *107*, 7812.
- Zhang, Z.; Imae, T. J. *Colloid Interface Sci.* **2001**, *233*, 107.
- Goutev, N.; Futamata, M. *Appl. Spectrosc.* **2003**, *57*, 506.
- Merklin, G. T.; Griffiths, P. R. *J. Phys. Chem. B* **1997**, *101*, 5810.
- Roy, D. *Opt. Commun.* **2001**, *200*, 119.
- Roy, D. *Appl. Spectrosc.* **2001**, *55*, 1046.
- Mielczarski, J. A.; Yoon, R. H. *J. Phys. Chem.* **1989**, *93*, 2034.
- Golden, W. G.; Saperstein, D. D.; Severson, M. W.; Overend, J. J. *Phys. Chem.* **1984**, *88*, 574.
- Barner, B. J.; Green, M. J.; Saez, E. I.; Corn, R. M. *Anal. Chem.* **1991**, *63*, 55–60.
- Dignam, M. J.; Moskovits, M.; Strobie, R. W. *Trans. Faraday Soc.* **1971**, *67*, 3306.
- Dignam, M. J.; Rao, B.; Moskovits, M.; Strobie, R. W. *Can. J. Chem.* **1971**, *49*, 1115.
- Azzam, R. M. A.; Bashara, N. M. *Ellipsometry and Polarized Light*; North-Holland: New York, 1999.
- Muller, R. H. In *Techniques for Characterization of Electrochemical Processes*; Varma, R., Selman, J. R., Eds.; John Wiley: New York, 1991; p 31.
- Hansen, W. N. *J. Opt. Soc. Am.* **1968**, *58*, 380.
- Hansen, W. N. *Symp. Faraday Soc.* **1970**, *4*, 27.
- McIntyre, J. D. E. In *Advances in Electrochemistry and Electrochemical Engineering*; Muller, R. H., Ed.; Wiley: New York, 1973; Vol. 9, p 61.
- Lynch, D. W.; Hunter, W. R. In *Handbook of Optical Constants of Solids*; Palik, E. D., Ed. Academic Press: New York, 1985; p 290.
- Osawa, M.; Ataka, K.-I. *Surf. Sci. Lett.* **1992**, *262*, L118.
- Aguilar, M.; Oliva, A. I.; Quintana, P.; Peña, J. L. *Surf. Sci.* **1997**, *380*, 91.
- Liu, Z. H.; Brown, N. M. D. *Thin Solid Films* **1997**, *300*, 84.
- He, L.; Shi, Z. Q. *Solid State Electron.* **1996**, *39*, 1996.
- Stobiński, L.; Zommer, L.; Duś, R. *Appl. Surf. Sci.* **1999**, *141*, 319.
- Nishikawa, Y.; Fujiwara, K.; Ataka, K.-I.; Osawa, M. *Anal. Chem.* **1993**, *65*, 556.
- Aspnes, D. E. *Thin Solid Films* **1982**, *89*, 249.
- Nikalasson, G. A.; Granqvist, G. C. *J. Appl. Phys.* **1984**, *55*, 3382.
- Allara, D. L.; Baca, A.; Pryde, C. A. *Macromolecules* **1978**, *11*, 1215.
- Bartell, L. S.; Churchill, D. J. *Phys. Chem.* **1961**, *65*, 2242.
- Parikh, A. N.; Allara, D. L. *J. Chem. Phys.* **1992**, *96*, 927.